APPLIED SCIENCES AND ENGINEERING

Curvilinear soft electronics by micromolding of metal nanowires in capillaries

Yuxuan Liu[1], Michael Zheng[1], Brendan O'Connor[1], Jingyan Dong[2], Yong Zhu[1,3,4,5]*

Soft electronics using metal nanowires have attracted notable attention attributed to their high electrical conductivity and mechanical flexibility. However, high-resolution complex patterning of metal nanowires on curvilinear substrates remains a challenge. Here, a micromolding-based method is reported for scalable printing of metal nanowires, which enables complex and highly conductive patterns on soft curvilinear and uneven substrates with high resolution and uniformity. Printing resolution of 20 μm and conductivity of the printed patterns of ~6.3 × 10^6 S/m are achieved. Printing of grid structures with uniform thickness for transparent conductive electrodes (TCEs) and direct printing of pressure sensors on curved surfaces such as glove and contact lens are also realized. The printed hybrid soft TCEs and smart contact lens show promising applications in optoelectronic devices and personal health monitoring, respectively. This printing method can be extended to other nanomaterials for large-scale printing of high-performance soft electronics.

INTRODUCTION

Flexible and stretchable soft electronics have emerged in recent years, enabling a broad spectrum of applications such as electronic skin, personal health monitoring and therapy, human-machine interfaces, plant wearables, and soft robotics (*1*–*11*). Soft conductor is one of the most important building blocks in soft electronics, such as electrodes for sensors and actuators, interconnects, and sensing elements. Nanomaterials such as carbon nanotubes (*8*, *12*), graphene (*4*, *13*, *14*), metal nanoparticles (NPs) (*15*–*17*), and metal nanowires (NWs) (*18*–*24*) have been used to construct soft conductors, typically compositing with polymer matrix. Among them, metal NWs show promising potentials for soft electronics.

Patterning techniques for metal NWs include lithography, mask-assisted patterning, laser-based patterning, and printing (*25*, *26*). Limitations exist for these techniques. For example, for printing techniques such as inkjet printing, screen printing, and gravure printing, polymer binders are usually added to the ink to modify the viscosity and surface tension. Hence, postprocessing is required to remove the polymer binders, which increases the process complexity and could damage the printed patterns and/or substrate. Furthermore, two challenges exist: patterning of grid structures and direct printing on curved surfaces. Grid structures made of metal NWs are widely used in transparent conductive electrodes (TCEs) (*27*, *28*). Noncontact printing techniques need multirun to script grid patterns, which results in uneven thickness at the crossing points. Direct printing of NWs on curved surfaces has not been reported using these two-dimensional (2D) patterning techniques.

Micromolding in capillary (MIMIC) has been developed for patterning polymer materials with high resolution (*29*–*31*). In this method, the ink, confined in a microchannel, is filled into the channel by capillary force automatically. Recently, this method has been used to print several materials including metal NWs (*32*–*35*). However, only simple patterns (e.g., straight lines) were printed on flat substrates with limited resolution and poor electric conductivity, and the substrates were limited to those with high surface energy (e.g., glass and plastics).

In this work, we report scalable printing of metal NWs for soft electronics using MIMIC with silver NWs (AgNWs) as an example. The printed AgNW patterns on elastomeric substrates show excellent resolution (20 μm), uniformity, conductivity (~6.3 × 10^6 S/m), and mechanical properties. The hydrodynamic behavior of the ink in the microchannel is investigated to achieve the desired filling velocity of the ink. Furthermore, a solution-based surface modification approach is used to enhance the adhesion between AgNWs and the elastomeric substrate, leading to higher uniformity and density of printed AgNWs. Printing of grid structures with uniform thickness and direct printing on curved surfaces including cylinders, hemispheres, and even arbitrary surfaces are achieved. Printing of AgNW grid structures is then demonstrated for the application of TCEs. Enabled by the capability of direct printing on curved surfaces, a wireless intraocular pressure (IOP) sensor is printed on a soft contact lens. The reported printing method offers several appealing features compared to other printing techniques: (i) The ink is formulated by AgNWs and solvent only without polymer binders, leading to high electric conductivity. (ii) This method can print grid structures with uniform thickness. (iii) Direct printing on curved and uneven surfaces can be achieved because the thin, stretchable mold can conform to such surfaces. (iv) The printing process is scalable (e.g., tens of centimeters long within minutes).

RESULTS

Overview of the printing

The MIMIC printing process is shown schematically in Fig. 1A. An ultraviolet (UV) photolithography step was used to pattern a photoresist film, on top of which liquid polydimethylsiloxane (PDMS) was poured and cured to form a PDMS mold with a microchannel for the subsequent MIMIC printing. Inlet and outlet were punched on the PDMS mold. AgNW/ethanol solution was used as the ink. The printing process starts with covering the PDMS mold facing down on the substrate and dropping AgNW ink at the inlet of the

[1]Department of Mechanical and Aerospace Engineering, North Carolina State University, Raleigh, NC 27695, USA. [2]Edward P. Fitts Department of Industrial and Systems Engineering, North Carolina State University, Raleigh, NC 27695, USA. [3]Joint Department of Biomedical Engineering, North Carolina State University, Raleigh, NC 27695, USA. [4]University of North Carolina at Chapel Hill, Chapel Hill, NC 27599, USA. [5]Department of Materials Science and Engineering, North Carolina State University, Raleigh, NC 27695, USA.
*Corresponding author. Email: yzhu7@ncsu.edu

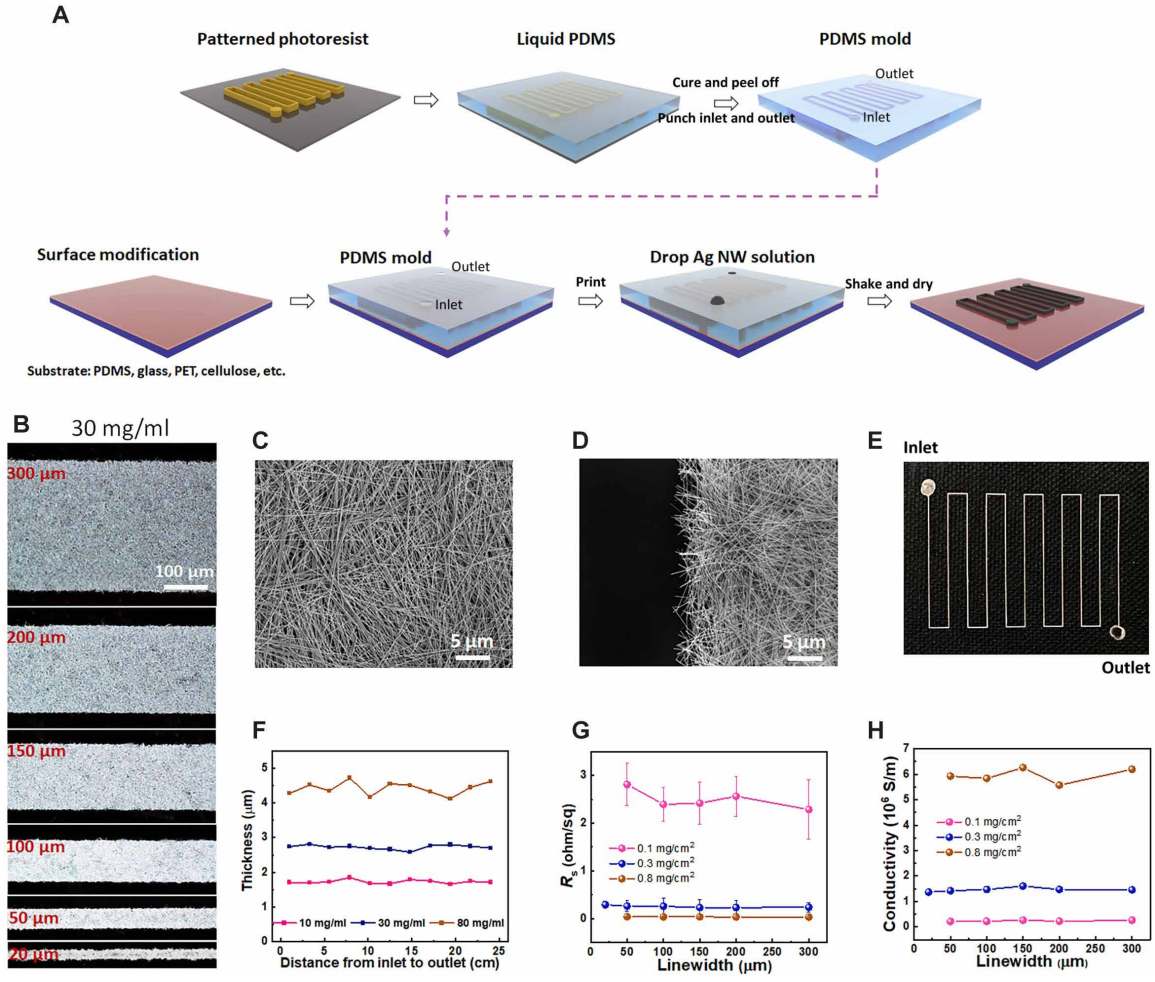

Fig. 1. Printing process and the printing performance. (**A**) Schematic diagram of the micromolding printing process. (**B**) Optical images of printed straight lines with linewidth ranging from 300 to 20 μm. Ink concentration: 30 mg/ml. SEM images of NWs (**C**) at the center and (**D**) along the edge of a printed pattern. (**E**) Printed serpentine structure. (**F**) Thickness of the printed serpentine structure, from the inlet to the outlet, with different ink concentrations. (**G**) Sheet resistance (R_s) and (**H**) electrical conductivity versus linewidth for the printed straight lines with different mass loading densities.

microchannel. Capillary pressure arising at the liquid-air interface in the microchannel introduces a negative sucking pressure, which pulls the ink flowing toward the outlet. After the ink fills the entire channel, the substrate and the mold are shaken until the solution is dried. After removing the mold, the pattern is successfully printed on the substrate.

The concentration of the ink can be controlled to print patterns with different AgNW densities and hence achieve different electrical properties. AgNW solutions with the concentration of 10, 30, and 80 mg/ml were used to print straight lines with linewidth ranging from 300 to 20 μm. The representative optical images of the printed lines using ink (30 mg/ml) are shown in Fig. 1B. The printed lines using inks with different concentrations are shown in fig. S1. The linewidth of the printed pattern is controlled by the width of the microchannel in the PDMS mold. Scanning electron microscopy (SEM) images of the center and the edge of a representative printed line are shown in Fig. 1 (C and D, respectively).

To study the thickness distribution along the printed line from the inlet to the outlet, a serpentine pattern as shown in Fig. 1E was printed. The thickness of printed AgNWs was measured at different locations along the pattern using a confocal microscope. The thickness distribution is shown in Fig. 1F, with no obvious differences from the inlet to the outlet for three inks of different concentrations. Figure S2 (A to C) shows the resistances, sheet resistances, and conductivities of the printed serpentine structure, from the inset to the outlet, with different ink concentrations. The sheet resistances and conductivities appear to be uniform along the pattern. This is because the ink reaches equilibrium after the microchannel is fully filled; that is, the ink is distributed uniformly along the entire channel after the filling process. Figure S2D shows the thickness as a function of the linewidth for different printed lines. It can be seen that the thickness of the printed lines is nearly constant irrespective of the linewidth. This feature is different from that of other printing methods such as inkjet printing and electrohydrodynamic printing, where the thickness (or loading density) typically changes with the linewidth (*36*, *37*). The mass loading density (per unit area) P can be defined as

$$P = \frac{C_{\text{ink}} \times \textit{Volume of the microchannel}}{\textit{Bottom area of the microchannel}} = \frac{C_{\text{ink}} \times l \times w \times h}{w \times l} = C_{\text{ink}} h \quad (1)$$

where l, w, and h are the length, width, and height of the microchannel and C_{ink} is the ink concentration. It can be seen that the mass loading density is only related to the ink concentration and the channel height (100 μm in this work).

The electrical properties of the printed lines with different linewidth and mass loading density P were investigated. Figure S2E and Fig. 1 (G and H) show the measured resistances, sheet resistances, and electrical conductivities of the printed lines, respectively. As shown in Fig. 1 (G and H), the sheet resistance and the conductivity depend only on the mass loading density P but not the linewidth. When the mass loading density was 0.8 mg/cm^2, the conductivity of the printed lines was as high as ~6.3 × 10^6 S/m without annealing, the highest among all the reported values for the conductivity of printed AgNW patterns (*25*).

Printing dynamics

The printing process consists of two steps: (i) ink filling driven by the capillary pressure at the liquid-air interface and (ii) NW settlement as a result of drying of the solvent. In the first step, relatively fast filling is needed to make sure that the ink goes through the whole channel quickly to avoid the NW accumulation at the liquid-air meniscus, which could cause channel blockage. The flow velocity in the microchannel u is given by the modified Washburn equation (*38*)

$$u \sim a\frac{P_c}{\mu x} \tag{2}$$

where a is a constant related to the geomertry of the microchannel, P_c is the capillary pressure at the liquid-air interface, μ is the viscosity of the ink, and x is the filling distance from the inlet. When the geometry of the microchannel is fixed, the filling velocity increases with the increase in P_c and decreases with the increase in μ and x. P_c can be calculated by (*38*)

$$P_c = \gamma\left(\frac{cos\,\theta_m + cos\,\theta_s}{w} + \frac{\theta_m}{h}\right) \tag{3}$$

where γ is the surface tension of the ink, θ_m is the contact angle between the ink and the mold, and θ_s is the contact angle between the ink and the substrate. Table S1 shows the physical properties of three typical solvents for AgNW inks and the calculated filling velocities at 2 and 30 cm in length (using glass as the substrate). It can be seen that water has a negative P_c due to the high contact angle and hence cannot drive the ink filling. Ethanol (or other alcohols such as methanol and isopropanol) has a small contact angle with PDMS (~20°), small contact angle with glass (~10°), and low viscosity, leading to a larger P_c and higher filling velocity u. Oil has similar P_c to ethanol, but the high viscosity makes the filling velocity too low. The ink filling process in a single path pattern can be found in movie S1. It took ~5 min to print the pattern of 25 cm long. Figure S3A shows the ink filling distance x as a function of the time, and fig. S3B shows the filling velocity u as a function of x. The experimental values of u are slightly smaller than the theoretical ones (see the Supplementary Materials), which is likely because the viscosity of pure ethanol used in the theoretical calculation is slightly smaller than that of the ethanol ink with AgNWs.

It is challenging to achieve high-uniformity patterning because of the low adhesion between the ink and the substrate (fig. S4) (*29*), which was addressed by a solution-based surface modification of the substrate (i.e., depositing a polydopamine layer on the PDMS substrate) (*39*). During ink drying, when the contact angle between the ink and the substrate is smaller than that between the ink and the mold walls (i.e., surface energy of the substrate is higher), the curvature of the meniscus at the ink-substrate interface is smaller than that at the ink-mold interface. Hence, the local liquid pressure at the substrate is higher according to Laplace's law, driving the ink to flow from the mold walls to the substrate, which contributes to settling of the NWs. After drying, high surface energy of the substrate also enhances adhesion between the NWs and the substrate, facilitating the NWs adhering to the substrate. Considering the strong van der Waals force between the NWs, once the first layer of NWs is adhered to the substrate, the rest of the NWs will form a stable 3D network structure. Note that typical surface treatment approaches for elastomers such as plasma and UVO-zone treatments are not ideal in the MIMIC printing case. The strong covalent siloxane bonds (Si—O—Si) formed between the elastomeric substrate and PDMS mold in such approaches would cause a cohesive failure when removing the mold after printing (*40*). The polydopamine thin film anchors the AgNWs via hydrogen bonds, which does not form overly strong bonds between the substrate and PDMS mold.

Edge accumulation of the NWs was also observed during the drying step, as shown in figs. S4 (E and F) and S5 (A and B). This is a result of the concave meniscus at the three-phase interface when the solvent evaporates. The ink stays longer at the lines of intersection between the mold and the substrate than that in the center. To prevent that, orbital shaking was found to be effective. Applying both the surface modification and orbital shaking, the printed AgNWs can be uniformly distributed with high density, as shown in fig. S4 (C, D, and G).

Electromechanical behavior

The printed line on the treated substrate with orbital shaking showed the best electromechanical behavior. Figure S6 shows the cyclic test results under 10 and 20% stretching for the unencapsulated printed lines. The resistance of the printed line remained stable within 200 cycles of 10% strain but started to show a large increase in less than 100 cycles when stretched to 20%. The effect of encapsulation on the electromechanical behavior of the printed lines was then evaluated (Fig. 2). The encapsulated lines showed enhanced failure strain and more stable resistance under stretching compared to the nonencapsulated ones (Fig. 2A). The resistance change under the loading-unloading strain of 20 and 50% in the first and second cycles is shown in Fig. 2B. The resistance after the first cycle did not reverse back to the original value because of the irreversible sliding between AgNWs in the PDMS matrix. Then, the resistance showed nearly reversible behavior attributed to the buckling of the NW/PDMS layer formed after the first cycle (*20*). The cyclic stability was also improved, as shown in Fig. 2C, where the resistance change remained constant in 400 cycles of 10 and 20% strain each.

Printed complex patterns

Complex patterns of AgNWs can be printed on a wide range of substrates, including curved or uneven ones, as long as the thin PDMS mold can conform to such substrates. Demonstrated substrates include glass, polyethylene terephthalate (PET), PDMS, cellulose film, latex glove, and plastic petri dish. Straight lines with different linewidths (Fig. 3A), horseshoe curve (Fig. 3B), serpentine curves (Fig. 3, C and D), grid structure (Fig. 3E), Peano curve (Fig. 3F), and spiral structure (Fig. 3G) were printed on a glass substrate. A rose

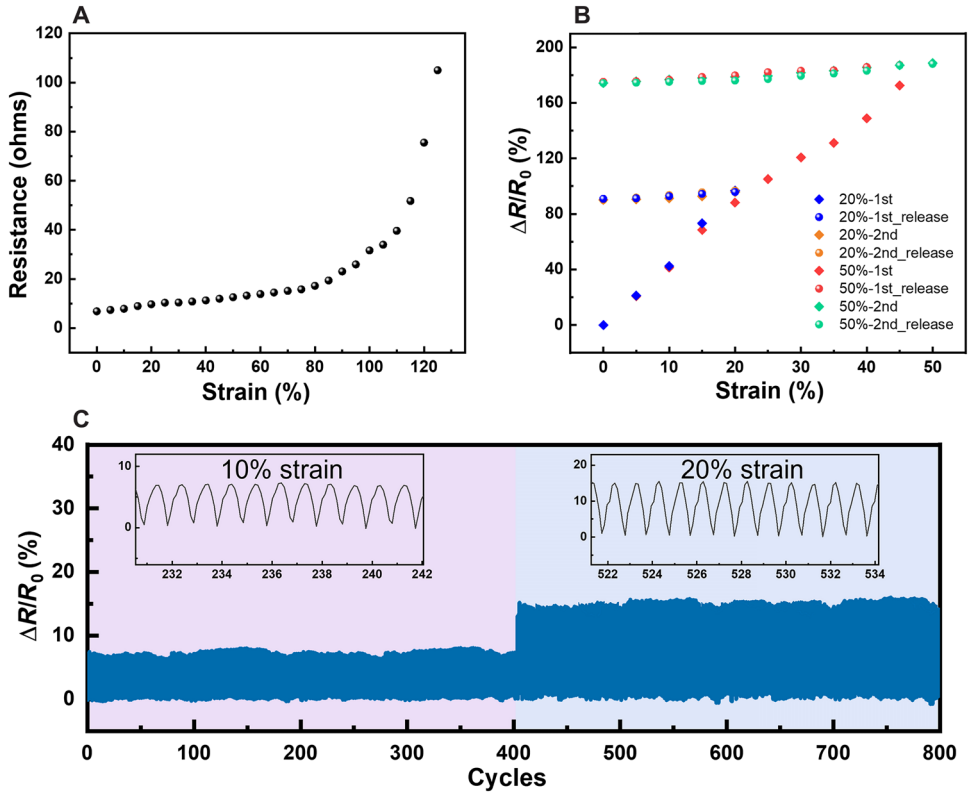

Fig. 2. Electromechanical behavior of the printed straight lines encapsulated by a thin PDMS layer. (**A**) Resistance versus applied strain. (**B**) Normalized resistance change versus applied strain in the first two cycles (strain rate: 1.8% per minute). (**C**) Change in resistance under cyclic strain of 10 and 20% for 800 cycles at a frequency of 1 Hz.

pattern was printed on a PDMS substrate, as shown in Fig. 3H. Integrated with two light-emitting diode (LED) lights and a power supply, a soft electronic circuit was built. The LED lights remained under stretching, as shown in fig. S7A. A serpentine and a grid structure were printed on a PET substrate, as shown in fig. S7B. Furthermore, this printing method can enable reliable printing on curvilinear surfaces such as developable (cylindrical) and nondevelopable (e.g., spherical) surfaces. For example, a glass test tube (Fig. 3I), a PDMS hemisphere (Fig. 3J), a glass round-bottom flask (fig. S7C), and a PDMS cylinder (fig. S7D) were used as the substrates for printing AgNW grid structures. This method can even print on arbitrary surfaces. As shown in Fig. 3K, a grid structure was printed across the bottom and the side of a glass teacup, where the bottom is concave and the side is convex. We further demonstrated the printing of grid structures on a saddle surface (the waist of a cat toy), a sloped surface, and a corrugated surface, as shown in Fig. 3 (L to O). Optical images of the curves, corners, and crossings on these complex patterns are shown in Fig. 3 (L to P), with magnified images showing the neat edges and uniform NW distribution. Complicated structures with gaps as small as <50 μm can be printed, as shown in fig. S8. 3D profiles of selected locations on the printed patterns including a corner, curve, and crossing are shown in fig. S9. The crossing area shows excellent uniformity in thickness.

Soft TCEs

Building on the capability of printing grid structures with uniform thickness, soft TCEs can be fabricated by printing commonly used grid structures such as square and hexagon. As shown in Fig. 4A, a square structured grid TCE with linewidth of 150 μm was printed on a glass substrate with good transparency and sheet resistance around 5 ohms per square. To further enhance the performance of the TCE, a random AgNW network can be spray-coated on the printed grid to form a hybrid structure. The flexible, hybrid TCEs were fabricated by embedding the hybrid structures in PDMS. For comparison, transmittances of the overall square structured hybrid TCE, the NW area on the grid, and the random NW network alone were measured to be ~82, 54, and 91%, respectively, as shown in Fig. 4C (grid linewidth, 150 μm; $P = 0.1$ mg/cm^2). The theoretical transmittance at 550-nm wavelength of the hybrid TCE T_h can be calculated on the basis of the transmittances of the random NW network alone T_{random} and the grid alone T_{grid} at 550-nm wavelength,

$$T_h = f_F \times T_{grid} + (1 - f_F) \times T_{random} \quad (4)$$

where f_F represents the filling factor of the grid, which can be calculated according to the geometry of the grid structure by (*41*, *42*)

$$f_F = \frac{L^2}{(L + W)^2} \quad (5)$$

where L is the side length of the square or the distance between two opposite sides of the hexagon in the grid structure and W is the linewidth of the grid structure.

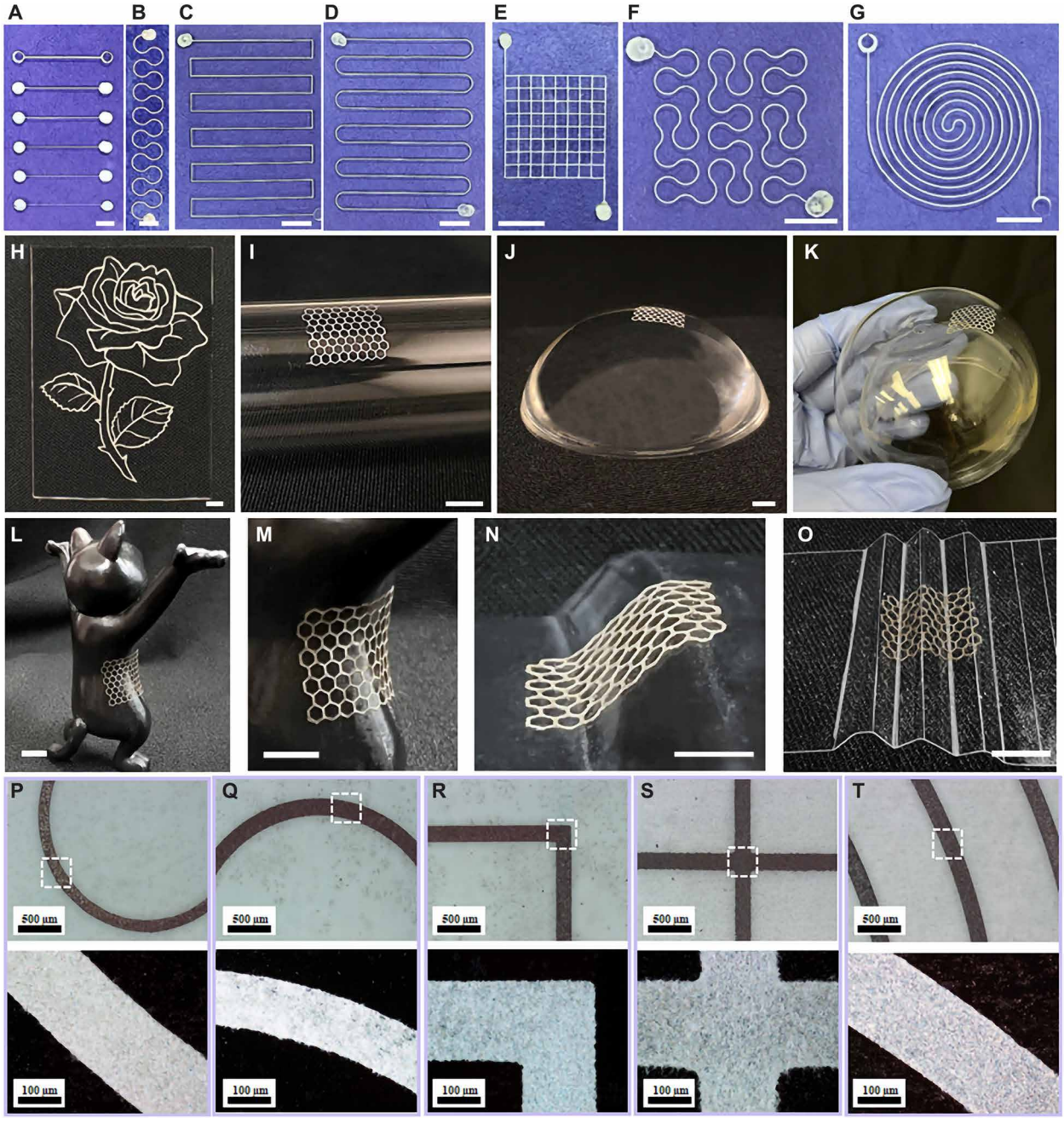

Fig. 3. Representative printed patterns. (**A**) Straight lines with different linewidths, (**B**) horseshoe pattern, (**C**) serpentine curve with right angle corners, (**D**) serpentine curve with round corners, (**E**) square grid structure, (**F**) Peano curve, (**G**) spiral structure, (**H**) rose pattern on PDMS, (**I**) grid structure on a glass tube, (**J**) hexagon grid structure on a PDMS hemisphere, and (**K**) hexagon grid structure across the bottom and the side of a glass teacup. (**L**) Printed hexagon grid structures on a saddle-shaped surface. (**M**) The magnified image of the printed pattern in (L). Printed hexagon grid structures on a (**N**) sloped surface and (**O**) corrugated surface. (A to G) On glass substrate. Scale bars, 5 mm (A to O). Optical images of (**P** and **Q**) curves, (**R**) corner, (**S**) crossing area in a grid structure, and (**T**) spiral structure. Top and bottom show low- and high-magnification images, respectively.

The theoretical transmittance value of the hybrid TCE at 550-nm wavelength is shown as the dashed line in Fig. 4C, very close to the experimental result (green line). SEM images indicate good connection between the printed grid and the spray-coated network, as shown in Fig. 4 (D and E), demonstrating that the MIMIC process is compatible with other coating methods such as spray coating. The optical images of the hybrid TCEs with different W are shown in Fig. 4F. Figure 4G shows the experimental and theoretical transmittances of the squared and hexagonal hybrid TCEs with different W at 550-nm wavelength. Figure 4H shows the experimental sheet resistances of these TCEs. The transmittance and the sheet resistance were found to decrease with the increase in W. The sheet resistance

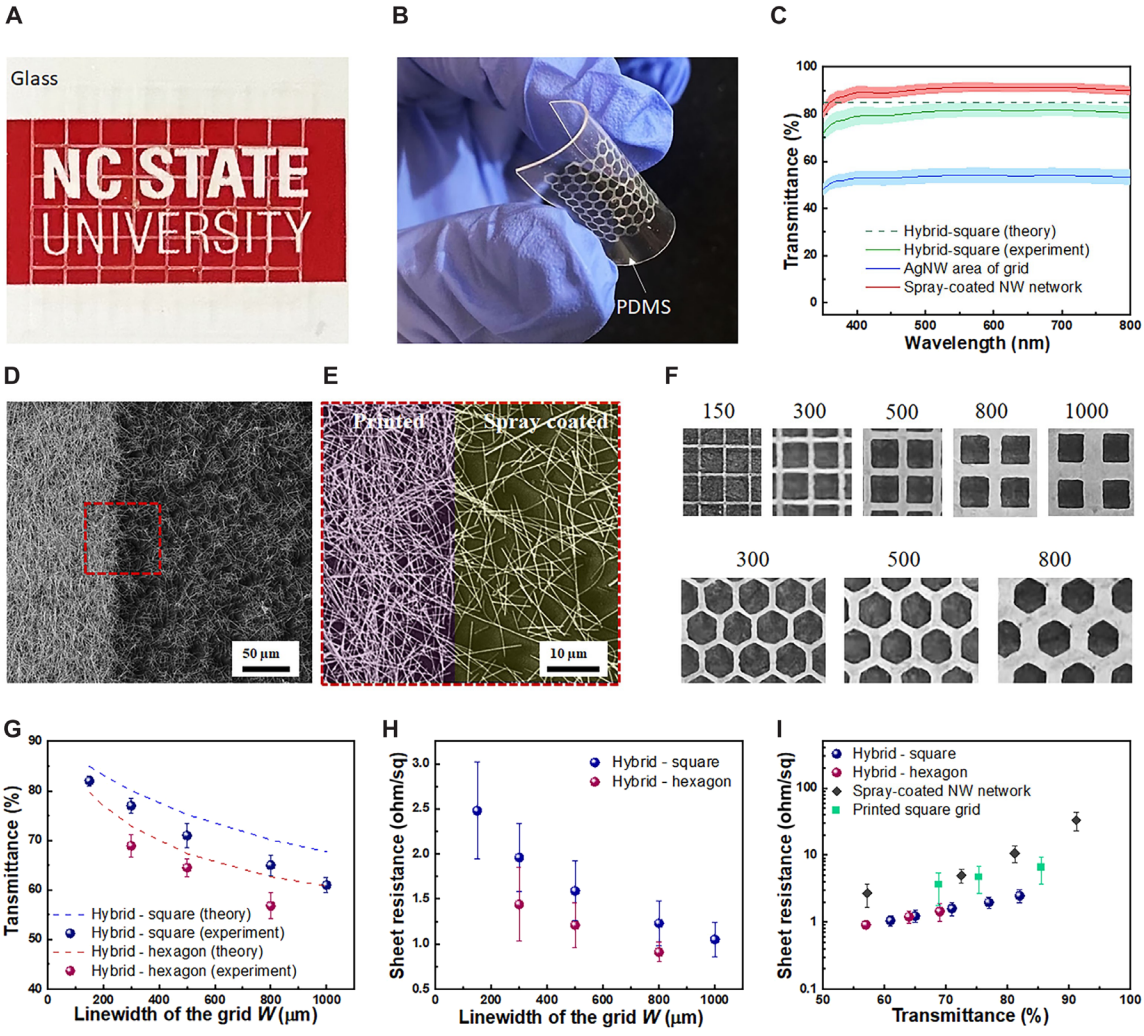

Fig. 4. Printed hybrid TCEs and their optoelectronic performance. (**A**) A grid structured TCE on a glass substrate. (**B**) A soft hybrid TCE with a hexagon structure on PDMS. (**C** and **D**) SEM images of the interface of the grid area and the spray-coated NW network area at different magnifications. (**E**) Transmittance of the pure spray-coated AgNW network, the NW area of the printed square grid structure, and the hybrid TCE. The dashed line represents the theoretical transmittance of the hybrid TCE at 550-nm wavelength. The error band represents the SD. (**F**) Optical images of the square and hexagon hybrid TCE with different linewidths *W* (as marked on top of the images, in micrometers) but fixed *L* of 1.5 mm. (**G**) Optical transmittance (theoretical and experimental) and (**H**) sheet resistance (experimental) versus the linewidth *W* of the hybrid TCEs with the square and hexagon structures (with fixed *L* of 1.5 mm). (**I**) The relationship between sheet resistance and transmittance of the spray-coated NW network, printed pure grid TCEs, and hybrid TCEs.

was as low as ~2.5 ohms per square when the transmittance was ~82%. The optoelectronic performances of the pure printed grid structure (square shape), the spray-coated NW network, and the hybrid structure were evaluated, as shown in Fig. 4I. It can be seen that the hybrid structured TCEs show enhanced optoelectronic performance compared to the pure grid structure and the random network.

Smart contact lens

Smart contact lens has attracted extensive interest because of its potential for wearable electronics to monitor various physical and chemical biosignals. For example, the increase in IOP is an important symptom of glaucoma; IOP monitoring would be of great importance in the diagnosis and treatment of glaucoma (*43*, *44*). However, fabrication of electronics on a contact lens is a challenge because of the curved surface (*45*–*47*). Taking the advantage of the capability of printing on curved surfaces, the MIMIC method was used to fabricate an IOP sensor directly on a soft contact lens. AgNWs were used as the piezoresistive sensor to detect the pressure change. Considering that the connection of lead wires for the data acquisition and the power source is impractical for contact lenses, wireless data/power transmission was exploited by printing an antenna on the contact lens, connected to the pressure sensor, which was coupled to an external antenna. To increase the sensitivity of the pressure sensor, the sensor was designed with a longer path (serpentine shape), low loading density (P = 0.03 mg/cm^2), and higher resistance (>1 kilohms), while the antenna was shorter (circle shape) with much higher loading density (P = 0.8 mg/cm^2) and lower resistance (~3 ohms). Figure 5 (A and B) shows the pressure sensor and the antenna printed on a commercially available contact lens. When the pressure applied on the smart contact lens changes, the

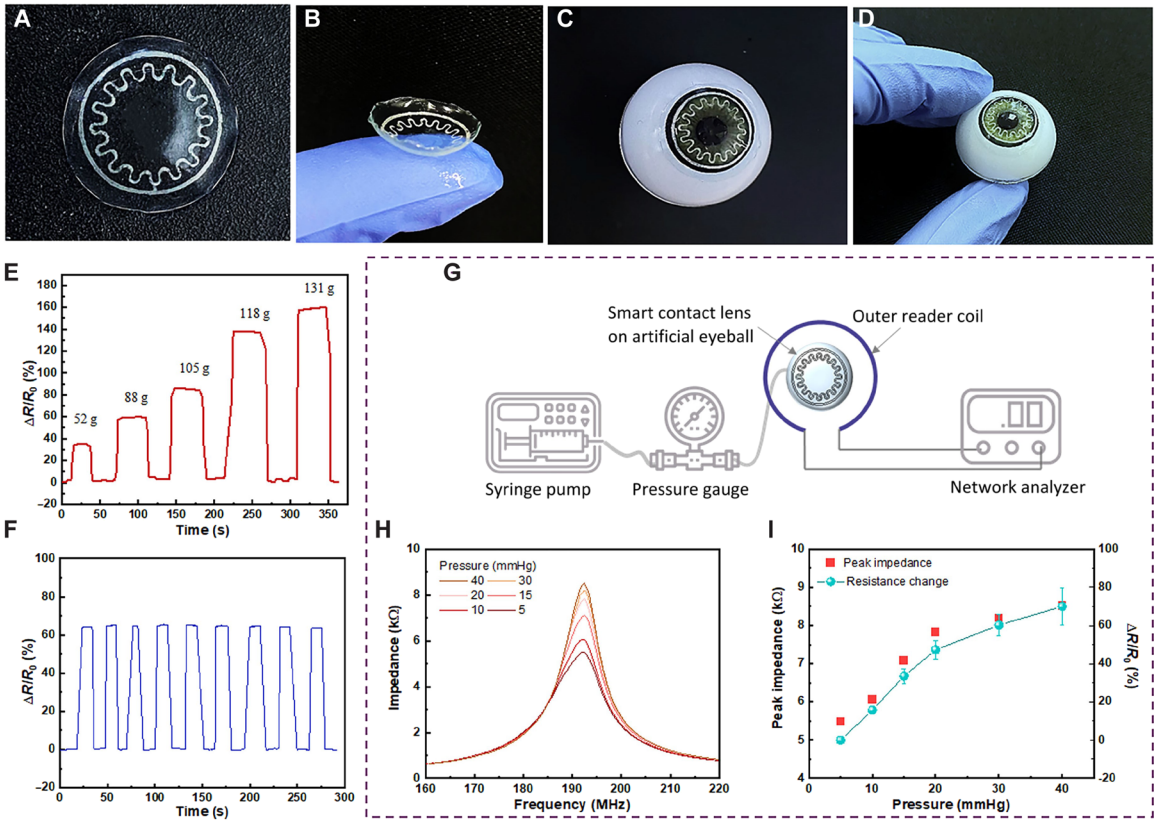

Fig. 5. Printed smart contact lens for IOP monitoring. (**A** and **B**) Printed smart contact lens with a pressure sensor (serpentine pattern) and an antenna (circle). (**C** and **D**) Smart contact lens on an artificial eyeball. (**E**) Resistance changes at different applied forces. (**F**) The resistance change under a cyclic loading (89.5*g* force). (**G**) Schematic illustration of the wireless IOP measurement system. (**H**) Frequency response of the impedance of the smart contact lens under applied internal pressure. (**I**) The maximum impedance and the resistance change of the smart contact lens under the applied internal pressure to the artificial eyeball ranging from 5 to 40 mmHg.

resistance of the piezoresistive sensor changes substantially, while the resistance of the antenna remains nearly constant. The fabricated smart contact lens was placed on an artificial eyeball with the same size as human eyeballs to demonstrate the wearability, as shown in Fig. 5 (C and D).

As shown in fig. S10A, a customized setup was used to measure the pressure response of the piezoresistive sensor. By pressing the soft artificial eyeball, the piezoresistive sensor was pressed, and the resistance of the sensor was recorded, as shown in Fig. 5E. Under the same force, the resistance change was reversible and stable (Fig. 5F). To carry out the wireless measurement, the smart contact lens was attached to the surface of the soft artificial eyeball, as shown in fig. S10B. The artificial eyeball was hollow in the center and filled with water to control the internal pressure. A schematic illustration and a picture of the measurement system are shown in Fig. 5G and fig. S10C, respectively. The smart contact lens was modeled as a parallel RLC resonance circuit, as shown in fig. S10D, consisting of resistance (R) of the piezoresistive sensor, inductance (L) of the antenna, and capacitance (C) formed between the piezoresistive sensor and the antenna. The impedance was measured by an impedance analyzer connected to the external antenna. When the internal pressure of the artificial eyeball increased, the resistance of the sensor increased, leading to the increase of the impedance. With the applied internal pressure ranging from 5 to 40 mmHg, the typical IOP of the human eyeball, the change of the impedance spectrum was recorded (Fig. 5H). The peak impedance increased with the increasing pressure, as shown in Fig. 5I. The resistance of the sensor was also monitored using a multimeter simultaneously (Fig. 5I). It can be seen that the impedance change is nearly proportional to the resistance change, indicating that the impedance change is mainly due to the resistance change. In addition to smart contact lens, direct printing of piezoresistive pressure sensors on a latex glove surface was also demonstrated (fig. S11).

DISCUSSION

In this work, we expanded the capabilities of the MIMIC method for scalable printing of AgNWs on a variety of substrates for soft electronics applications. To improve the printing performance, we carefully studied the fundamentals of fluid dynamics in the microchannel. Surface modification was conducted to improve the fluid dynamics and the AgNW settlement; orbital shaking was used to address the AgNW edge accumulation problem during the drying of the ink, and proper solvent was chosen to ensure sufficient capillary force. The morphology, electrical properties, and mechanical properties are investigated to optimize the printing process. We demonstrate the printing resolution of 20 μm and the conductivity of the printed patterns of ~6.3×10^6 S/m. This printing method

has several distinct features: (i) The mass loading density, thickness, and electric properties of the printed patterns only depend on the ink concentration and the microchannel height, not on other parameters such as linewidth; (ii) printing of a grid structure with uniform thickness across the entire structure including crossing points; and (iii) direct printing on curved and uneven surfaces as long as the thin PDMS mold can conform to the surfaces. Taking advantage of these features, deformable hybrid TCEs, distributed pressure sensors on a glove, and smart contact lenses with a pressure sensor are directly printed. The printed hybrid TCEs can achieve sheet resistance as low as ~2.5 ohms per square with the optical transmittance of ~82%, and the IOP of an artificial eyeball can be measured by wirelessly monitoring the impedance of the pressure sensor printed on the smart contact lens. The micromolding printing strategy proposed here provides a flexible, versatile approach for fabricating 3D soft electronics and sensors.

The reported printing approach has outstanding printing efficiency. In terms of material efficiency, the micromolding-based patterning approach, as an additive manufacturing method, can save ink materials compared to subtractive methods. In addition, the PDMS mold is reusable. In terms of energy efficiency, the micromolding-based method does not require an external driving force during the printing and heating or light exposure during the postprocessing. Filling of the ink is spontaneous, and drying of the solvent is at room temperature. As a result, the patterning process does not consume additional energy. In terms of time efficiency, the filling process of the ink is quite fast, typically taking several minutes to fill in a 25-cm-long channel. The dying process is around 30 min. The printing speed and postprocess time are both comparable to those of other patterning methods such as inkjet-based printing. Compared to homogeneous inks such as polymers (*31*) and liquid metal (*35*), AgNW ink is heterogeneous with AgNWs and solvent in the ink, which is more challenging to print using micromolding-based approaches. Compared to other molding approaches (*48*, *49*), the reported printing approach does not use polymer additives to adjust the ink viscosity, which increases the electrical conductivity and avoids complicated postprocessing. The approach can be used not only for metal NWs but also for other nanomaterials such as metal NPs, carbon nanotubes, and 2D materials.

MATERIALS AND METHODS

Fabrication of PDMS mold

The PDMS mold used for the printing can be fabricated by two approaches. For the lithography-based approach, UV lithography was used to pattern the SU-8 photoresist on a silicon wafer using a PET photomask, where the thickness of the photoresist was 100 μm, which defines the height of the fabricated microchannel. Then, the liquid PDMS mixture (SYLGARD 184, Dow Corning, with a weight ratio of silicone elastomer to curing agent of 10 to 1) was poured onto the patterned photoresist and spin-coated at 300 rpm to form a 200-μm-thickness film. After curing the PDMS at 80°C for 2 hours, the PDMS mold was peeled off from the silicon wafer, and the inlet and outlet were punched at the designed locations by a stainless-steel hole puncher. For the nonlithography-based approach, the pattern was scribed by a CO_2 laser cutter on Kapton tape with the desired thickness, and then, the PDMS mixture was poured onto the patterned Kapton tape. The resolution of the nonlithography process is lower than that of lithography, e.g., 100 μm compared to 10 μm.

Surface modification of PDMS substrate

Surface modification of the low–surface energy substrate such as PDMS was carried out using a previously reported method (*39*). Typically, polydopamine/tris-HCl buffer (pH 8.5) was used to immerse the substrate for 15 min, and then, the substrate was cleaned using N_2 flow. After drying the substrate in the air at 80°C for 1 hour, a thin layer of polydopamine was cross-linked on the surface.

Printing of AgNWs

The AgNWs were synthesized by a modified polyol method (*50*). Before printing, the substrate was cleaned using N_2 flow. To start the printing, the mold was placed on the clean substrate and pressed gently to ensure conformal contact with the substrate. Then, 50 to 200 μl of ink were dropped into the inlet depending on the length and the linewidth of the pattern. After the ink filled the entire microchannel, the whole setup, including the mold, substrate, and ink in the channel, was transferred to an orbital shaker and shaken at 500 rpm at room temperature for 30 min to 1 hour until the ink dried. Then, the PDMS mold was removed, and the pattern was successfully printed. For encapsulated samples, another layer of PDMS mixture was spin-coated on top of the printed pattern at 2000 rpm and cured at 80°C for 2 hours to form an encapsulation layer of ~25 μm.

Characterization of printed patterns

The thickness of the printed patterns was measured using a Keyence confocal microscope. For every sample, five locations were measured, and the average thickness was calculated. The optical laser microscope images, the 3D contour images, and the profiles of the measured patterns were collected. The printed patterns were also characterized by an optical microscope (Nikon Polarizing Microscope ECLIPSE LV100N) and SEM (Thermo Fisher Scientific Quanta 3D FEG). The resistance of the printed lines was measured by the typical four-probe method using a multimeter. The length of the printed lines was 2 cm for all the measurement. The sheet resistance R_s was calculated by $R_s = \frac{Rw}{L}$, where R is the measure resistance, w is the linewidth, and L is the length of the measured line. The electrical conductivity σ of the printed patterns was calculated by $\sigma = \frac{1}{R_s t}$, where t is the thickness of the printed line.

Fabrication and characterization of soft TCEs

To fabricate soft hybrid TCEs, the grid structures with different W and a fixed L of 1.5 mm (for both square and hexagon) were first printed on a glass substrate with a mass loading density of 0.1 mg/cm^2. Then, the random NW network was spray-coated on the printed grids using ink (1 mg/ml) for 12 s. The sheet resistance of the printed grid mesh was calculated by the Van der Pauw method with $R_s = \frac{\pi R}{ln2}$, where R is the measured average resistance in the vertical direction and the horizontal direction. The transmittance of the TCEs was measured using a UV–visible spectrophotometer (SpectraMax). Forty different locations on each TCE were scanned, and the average transmittance was calculated. The transmittance of the NW grid area on the hybrid TCE was measured at the crossing area on the grid. The spot size of the laser beam is about 0.5 mm by 0.5 mm. A sample with grid linewidth of 1 mm was measured to represent the transmittance of the NW grid area on the hybrid TCE. To fabricate TCEs with pure grid structure having different transmittance and sheet

resistance, grid structures with different W (300, 500, and 1000 μm) and a fixed L of 1.5 mm were printed. To fabricate TCEs with random NW network having different transmittance and sheet resistance, AgNW solution (1 mg/ml) was spray-coated on glass substrates for different durations (12, 30, 60, and 120 s).

Fabrication of smart contact lens

The soft contact lens used to fabricate smart contact lenses is commercially available (Acuvue Oasys). To print on the soft contact lens, the soft contact lens was first placed on a rigid artificial eyeball made of acrylic. Then, a PDMS mold larger than the soft contact lens was covered on the contact lens. After the printing, a thin layer of PDMS was cast on the contact lens to encapsulate the printed patterns. The fabricated smart contact lens was stored in a contact lens solution to keep the moisture.

SUPPLEMENTARY MATERIALS

Supplementary material for this article is available at https://science.org/doi/10.1126/sciadv.add6996

REFERENCES AND NOTES

1. S. Yao, P. Swetha, Y. Zhu, Nanomaterial-enabled wearable sensors for healthcare. *Adv. Healthc. Mater.* **7**, 1700889 (2018).
2. S. Xu, Y. Zhang, L. Jia, K. E. Mathewson, K.-I. Jang, J. Kim, H. Fu, X. Huang, P. Chava, R. Wang, S. Bhole, L. Wang, Y. J. Na, Y. Guan, M. Flavin, Z. Han, Y. Huang, J. A. Rogers, Soft microfluidic assemblies of sensors, circuits, and radios for the skin. *Science* **344**, 70–74 (2014).
3. S. I. Rich, R. J. Wood, C. Majidi, Untethered soft robotics. *Nat. Electron.* **1**, 102–112 (2018).
4. H. Lee, T. K. Choi, Y. B. Lee, H. R. Cho, R. Ghaffari, L. Wang, H. J. Choi, T. D. Chung, N. Lu, T. Hyeon, S. H. Choi, D.-H. Kim, A graphene-based electrochemical device with thermoresponsive microneedles for diabetes monitoring and therapy. *Nat. Nanotechnol.* **11**, 566–572 (2016).
5. S. Niu, N. Matsuhisa, L. Beker, J. Li, S. Wang, J. Wang, Y. Jiang, X. Yan, Y. Yun, W. Burnett, A. S. Y. Poon, J. B.-H. Tok, X. Chen, Z. Bao, A wireless body area sensor network based on stretchable passive tags. *Nat. Electron.* **2**, 361–368 (2019).
6. M. Kaltenbrunner, T. Sekitani, J. Reeder, T. Yokota, K. Kuribara, T. Tokuhara, M. Drack, R. Schwödiauer, I. Graz, S. Bauer-Gogonea, S. Bauer, T. Someya, An ultra-lightweight design for imperceptible plastic electronics. *Nature* **499**, 458–463 (2013).
7. S. Wang, J. Xu, W. Wang, G.-J. N. Wang, R. Rastak, F. Molina-Lopez, J. W. Chung, S. Niu, V. R. Feig, J. Lopez, T. Lei, S.-K. Kwon, Y. Kim, A. M. Foudeh, A. Ehrlich, A. Gasperini, Y. Yun, B. Murmann, J. B.-H. Tok, Z. Bao, Skin electronics from scalable fabrication of an intrinsically stretchable transistor array. *Nature* **555**, 83–88 (2018).
8. D. J. Lipomi, M. Vosgueritchian, B. C.-K. Tee, S. L. Hellstrom, J. A. Lee, C. H. Fox, Z. Bao, Skin-like pressure and strain sensors based on transparent elastic films of carbon nanotubes. *Nat. Nanotechnol.* **6**, 788–792 (2011).
9. D. H. Kim, N. Lu, R. Ma, Y.-S. Kim, R.-H. Kim, S. Wang, J. Wu, S. M. Won, H. Tao, A. Islam, K. J. Yu, T. Kim, R. Chowdhury, M. Ying, L. Xu, M. Li, H.-J. Chung, H. Keum, M. M. Cormick, P. Liu, Y.-W. Zhang, F. G. Omenetto, Y. Huang, T. Coleman, J. A. Rogers, Epidermal electronics. *Science* **333**, 838–843 (2011).
10. W. Li, N. Matsuhisa, Z. Liu, M. Wang, Y. Luo, P. Cai, G. Chen, F. Zhang, C. Li, Z. Liu, Z. Lv, W. Zhang, X. Chen, An on-demand plant-based actuator created using conformable electrodes. *Nat. Electron.* **4**, 134–142 (2021).
11. Z. Li, Y. Liu, O. Hassain, R. Paul, S. Yao, S. Wu, J. B. Ristaino, Y. Zhu, Q. Wei, Real-time monitoring of plant stresses via chemiresistive profiling of leaf volatiles by a wearable sensor. *Matter* **4**, 2553–2570 (2021).
12. A. J. Bandodkar, I. Jeerapan, J.-M. You, R. Nunes-Flores, J. Wang, Highly stretchable fully-printed cnt-based electrochemical sensors and biofuel cells: Combining intrinsic and design-induced stretchability. *Nano Lett* **16**, 721–727 (2016).
13. S. Kabiri, Graphene electronic tattoo sensors. *ACS Nano* **11**, 7634–7641 (2017).
14. M. Kang, M. Kang, J. Kim, B. Jang, Y. Chae, J.-H. Kim, J.-H. Ahn, Graphene-based three-dimensional capacitive touch sensor for wearable electronics. *ACS Nano* **11**, 7950–7957 (2017).
15. Y. Khan, M. Garg, Q. Gui, M. Schadt, A. Gaikwad, D. Han, N. A. D. Yamamoto, P. Hart, R. Welte, W. Wilson, S. Czarnecki, M. Poliks, Z. Jin, K. Ghose, F. Egitto, J. Turner, A. C. Arias, Flexible hybrid electronics: Direct interfacing of soft and hard electronics for wearable health monitoring. *Adv. Funct. Mater.* **26**, 8764–8775 (2016).
16. H. Jin, T.-P. Huynh, H. Haick, Self-healable sensors based nanoparticles for detecting physiological markers via skin and breath: Toward disease prevention via wearable devices. *Nano Lett* **16**, 4194–4202 (2016).
17. M. Park, J. Im, M. Shin, Y. Min, J. Park, H. Cho, S. Park, M.-B. Shim, S. Jeon, D.-Y. Chung, J. Bae, J. Park, U. Jeong, K. Kim, Highly stretchable electric circuits from a composite material of silver nanoparticles and elastomeric fibres. *Nat. Nanotechnol.* **7**, 803–809 (2012).
18. W. Zhou, S. Yao, H. Wang, Q. Du, Y. Ma, Y. Zu, Gas-permeable, ultrathin, stretchable epidermal electronics with porous electrodes. *ACS Nano* **14**, 5798–5805 (2020).
19. S. Yao, A. Myers, A. Malhotra, F. Lin, A. Bozkurt, J. F. Muth, Y. Zhu, A wearable hydration sensor with conformal nanowire electrodes. *Adv. Healthc. Mater.* **6**, 1601159 (2017).
20. F. Xu, Y. Zhu, Highly conductive and stretchable silver nanowire conductors. *Adv. Mater.* **24**, 5117–5122 (2012).
21. S. Hong, H. Lee, J. Lee, J. Kwon, S. Han, Y. D. Suh, H. Cho, J. Shin, J. Yeo, S. H. Ko, Highly stretchable and transparent metal nanowire heater for wearable electronics applications. *Adv. Mater.* **27**, 4744–4751 (2015).
22. P. Song, H. Qin, H. L. Gao, H. P. Cong, S. H. Yu, Self-healing and superstretchable conductors from hierarchical nanowire assemblies. *Nat. Commun.* **9**, 2786 (2018).
23. J. Liang, K. Tong, Q. Pei, A water-based silver-nanowire screen-print ink for the fabrication of stretchable conductors and wearable thin-film transistors. *Adv. Mater.* **28**, 5986–5996 (2016).
24. S. Gong, W. Schwalb, Y. Wang, Y. Chen, Y. Tang, J. Si, B. Shirinzadeh, W. Cheng, A wearable and highly sensitive pressure sensor with ultrathin gold nanowires. *Nat. Commun.* **5**, 3132 (2014).
25. Q. Huang, Y. Zhu, Patterning of metal nanowire networks: Methods and applications. *ACS Appl. Mater. Interfaces* **13**, 60736–60762 (2021).
26. R. Zhang, J. Jiang, W. Wu, Scalably nanomanufactured atomically thin materials-based wearable health sensors. *Small Struct.* **3**, 2100120 (2021).
27. S. Han, M. K. Kim, B. Wang, D. S. Wie, S. Wang, C. H. Lee, Mechanically reinforced skin-electronics with networked nanocomposite elastomer. *Adv. Mater.* **28**, 10257–10265 (2016).
28. P. C. Hsu, S. Wang, H. Wu, V. K. Narasimhan, D. Kong, H. R. Lee, Y. Cui, Performance enhancement of metal nanowire transparent conducting electrodes by mesoscale metal wires. *Nat. Commun.* **4**, 2522 (2013).
29. E. Kim, Y. Xia, G. M. Whitesides, Polymer microstructures formed by moulding in capillaries. *Nature* **376**, 581–584 (1995).
30. X.-M. Zhao, Y. Xia, G. M. Whitesides, Soft lithographic methods for nano-fabrication. *J. Mater. Chem.* **7**, 1069–1074 (1997).
31. X.-M. Zhao, A. Stoddart, S. P. Smith, E. Kim, Y. Xia, M. Prentiss, G. M. Whitesides, Fabrication of single-mode polymeric waveguides using micromolding in capillaries. *Adv. Mater.* **8**, 420–424 (1996).
32. B. Ha, S. Jo, Hybrid Ag nanowire transparent conductive electrodes with randomly oriented and grid-patterned Ag nanowire networks. *Sci. Rep.* **7**, 11614 (2017).
33. Q. He, H. G. Sudibya, Z. Yin, S. Wu, H. Li, F. Boey, W. Huang, P. Chen, H. Zhang, Centimeter-long and large-scale micropatterns of reduced graphene oxide films: Fabrication and sensing applications. *ACS Nano* **4**, 3201–3208 (2010).
34. S. Hu, J. Gu, W. Zhao, H. Ji, X. Ma, J. Wei, M. Li, Silver-nanowire mesh-structured transparent conductive film with improved transparent conductive properties and mechanical performance. *Adv. Funct. Mater.* **4**, 1900194 (2019).
35. T. H. Park, J.-H. Kim, S. Seo, Facile and rapid method for fabricating liquid metal electrodes with highly precise patterns via one-step coating. *Adv. Funct. Mater.* **30**, 2003694 (2020).
36. D. J. Finn, M. Lotya, J. N. Coleman, Inkjet printing of silver nanowire networks. *ACS Appl. Mater. Interfaces* **7**, 9254–9261 (2015).
37. Z. Cui, Y. Han, Q. Huang, J. Dong, Y. Zhu, Electrohydrodynamic printing of silver nanowires for flexible and stretchable electronics. *Nanoscale* **10**, 6806–6811 (2018).
38. A. Olanrewaju, M. Beaugrand, M. Yafia, D. Juncker, Capillary microfluidics in microchannels: From microfluidic networks to capillaric circuits. *Lab Chip* **18**, 2323–2347 (2018).
39. P. Ren, Y. Liu, R. Song, B. O'Connor, J. Dong, Y. Zhu, Achieving high-resolution electrohydrodynamic printing of nanowires on elastomeric substrates through surface modification. *ACS Appl. Electron. Mater.* **3**, 192–202 (2020).
40. A. Borok, K. Laboda, A. Bonyar, PDMS bonding technologies for microfluidic applications: A review. *Biosensors* **11**, 292 (2021).
41. I. Khan, S. Castelletto, G. Rosengarten, A novel hexagonal beam steering electrowetting device for solar energy concentration. *Micromachines* **11**, 1016 (2020).
42. H. B. Lee, W.-Y. Jin, M. M. Ovhal, N. Kumar, J.-W. Kang, Flexible transparent conducting electrodes based on metal meshes for organic optoelectronic device applications: A review. *J. Mater. Chem. C.* **7**, 1087–1110 (2019).
43. A. Heijl, M. C. Leske, B. Bengtsson, L. Hyman, B. Bengtsson, M. Hussein; Early Manifest Glaucoma Trial Group, Reduction of intraocular pressure and glaucoma progression: Results from the early manifest glaucoma trial. *Arch. Ophthalmol.* **120**, 1268–1279 (2002).

44. J. Kim, J. Park, Y.-G. Park, E. Cha, M. Ku, H. S. An, K.-P. Lee, M.-I. Huh, J. Kim, T.-S. Kim, D. W. Kim, H. K. Kim, J.-U. Park, A soft and transparent contact lens for the wireless quantitative monitoring of intraocular pressure. *Nat. Biomed. Eng.* **5**, 772–782 (2021).
45. I. Jung, J. Xiao, V. Malyarchuk, C. Lu, M. Li, Z. Liu, J. Yoon, Y. Huang, J. A. Rogers, Dynamically tunable hemispherical electronic eye camera system with adjustable zoom capability. *Proc. Natl. Acad. Sci. U.S.A.* **108**, 1788–1793 (2011).
46. J. Park, J. Kim, S.-Y. Kim, W. H. Cheong, J. Jang, Y.-G. Park, K. Na, Y.-T. Kim, J. H. Heo, C. Y. Lee, J. H. Lee, F. Bien, J.-U. Park, Soft, smart contact lenses with integrations of wireless circuits, glucose sensors, and displays. *Sci. Adv.* **4**, eaap9841 (2011).
47. X. Ma, S. Ahadian, S. Liu, J. Zhang, S. Liu, T. Cao, W. Lin, D. Wu, N. R. de Barros, M. R. Zare, S. E. Diltemiz, V. Jucaud, Y. Zhu, S. Zhang, E. Banton, Y. Gu, K. Nan, S. Xu, M. R. Dokmeci, A. Khademhosseini, Smart contact lenses for biosensing applications. *Adv. Intell. Syst.* **3**, 2000263 (2021).
48. M. Namkoong, H. Guo, M. S. Rahman, D. Wang, C. J. Pfeil, S. Hager, L. Tian, Moldable and transferrable conductive nanocomposites for epidermal electronics. *npj Flex. Electron.* **6**, 41 (2022).
49. J. Park, S. Choi, A. H. Janardhan, S.-Y. Lee, S. Raut, J. Soares, K. Shin, S. Yang, C. Lee, K.-W. Kang, H. R. Cho, S. J. Kim, P. Seo, W. Hyun, S. Jung, H.-J. Lee, N. Lee, S. H. Choi, M. Sacks, N. Lu, M. E. Josephson, T. Hyeon, D.-H. Kim, H. J. Hwang, Electromechanical cardioplasty using a wrapped elasto-conductive epicardial mesh. *Sci. Transl. Med.* **8**, 344ra86 (2016).
50. K. E. Korte, S. E. Skrabalak, Y. Xia, Rapid synthesis of silver nanowires through a CuCl- or $CuCl_2$-mediated polyol process. *J. Mater. Chem.* **18**, 437–441 (2008).
51. Y. Zhu, K. Petkovic-Duran, Capillary flow in microchannels. *Microfluid. Nanofluid.* **8**, 275–282 (2010).
52. S. Yao, Y. Zhu, Wearable multifunctional sensors using printed stretchable conductors made of silver nanowires. *Nanoscale* **6**, 2345–2352 (2014).

Acknowledgments

Funding: We would like to acknowledge the NSF for the financial support under award nos. 1728370 and 2134664. **Author contributions:** Y.L. and Y.Z. conceived the idea and designed all the experiments. Y.L. conducted all the experiments and data analysis. M.Z. helped with the printing experiments. B.O. and J.D. contributed to the discussion and provided valuable suggestions. Y.L. and Y.Z. wrote the manuscript with inputs from all the authors. **Competing interests:** The authors declare that they have no competing interests. **Data and materials availability:** All data needed to evaluate the conclusions in the paper are present in the paper and/or the Supplementary Materials.

Submitted 28 June 2022
Accepted 3 October 2022
Published 18 November 2022
10.1126/sciadv.add6996